HHS Public Access

Author manuscript

Neuroimage. Author manuscript; available in PMC 2019 January 15.

Published in final edited form as:

Neuroimage. 2018 January 15; 165: 251–264. doi:10.1016/j.neuroimage.2017.09.055.

Long-term Optical Imaging of Neurovascular Coupling in Mouse Cortex Using GCaMP6f and Intrinsic Hemodynamic Signals

Xiaochun Gu[a,b], **Wei Chen**[a], **Jiang You**[a], **Alan P. Koretsky**[c], **N. D. Volkow**[d], **Yingtian Pan**[a], and **Congwu Du**[a,*]

[a]Department of Biomedical Engineering, Stony Brook University, Stony Brook, NY 11794, USA

[b]Jiangsu Key Laboratory of Molecule Imaging and Functional Imaging, Key Laboratory of Developmental Genes and Human Diseases, MOE, Department of Histology and Embryology, School of Medicine, Southeast University, Nanjing, 210009, PR China

[c]Laboratory of Functional and Molecular Imaging, National Institute of Neurological Disorders and Stroke, National Institutes of Health, Bethesda, MD 20892, USA

[d]National Institute on Alcohol Abuse and Alcoholism, National Institutes of Health, Bethesda, MD 20857, USA

Summary

Cerebral hemodynamics is modulated in response to changes in neuronal activity, a process termed neurovascular coupling (NVC), which can be disrupted by neuropsychiatric diseases (e.g., stroke, Alzheimer's disease). Thus, there is growing interest to image long-term NVC dynamics with high spatiotemporal resolutions. Here, by combining the use of a genetically-encoded calcium indicator with optical techniques, we develop a longitudinal multimodal optical imaging platform (MIP) that enabled time-lapse tracking of NVC over a relatively large field of view in the mouse somatosensory cortex at single cell and single vessel resolutions. Specifically, GCaMP6f was used as marker of neuronal activity, which along with MIP allowed us to simultaneously measure the changes in neuronal $[Ca^{2+}]_i$ fluorescence, cerebral blood flow velocity (CBFv) and hemodynamics longitudinally for more than eight weeks. We show that $[Ca^{2+}]_i$ fluorescence was detectable one week post viral injection and the damage to local microvasculature and perfusion recovered two weeks after injection. By three weeks post viral injection, maximal neuronal and CBFv responses to hindpaw stimulations were observed. Moreover, single neuronal activation in response to hindpaw stimulation was consistently recorded, followed by ~2 second delayed dilation of

*During review process, please address correspondence to: Congwu Du, PhD, Professor, Department of Biomedical Engineering, State University of New York at Stony Brook, Life Science Bldg, Rm. 002, Stony Brook, NY 11794-5281, Tel: (631) 632-5480 (Office), (631) 632-5481 (Lab), Congwu.Du@stonybrook.edu.

Author Contributions

X.G., C.D., and Y.P. designed research; X.G., J.Y and W.C. carried out the experiments and data analysis; and X.G., C.D., Y.P. and N.D.V. and A.K. contributed significantly to discussing the results and writing the manuscript.

Conflict of interest

The authors declare no competing financial interests.

contiguous microvessels. Additionally, resting-state spontaneous neuronal and hemodynamic oscillations were detectable throughout the eight weeks of study. Our results demonstrate the capability of MIP for longitudinal investigation of the organization and plasticity of the neurovascular network during resting state and during stimulation-evoked neuronal activation at high spatiotemporal resolutions.

Keywords

longitudinal imaging; GCaMP6f; Rest state; Cerebral blood flow; Simultaneous optical detection; Neurovascular coupling

1. Introduction

Neurovascular Coupling (NVC) is the process by which local cerebral blood flow (CBF) is modulated to meet the energy demands from regional neuronal activity (Raichle, 1998). Disruption of NVC leads to neuropathology and it has been reported in stroke and neurodegenerative conditions such as Alzheimer's disease (Girouard and Iadecola, 2006; Hamilton et al., 2010). Most of the main functional imaging techniques rely on NVC to infer changes in neuronal activity, for example, fMRI measures blood-oxygenation level dependent (BOLD) signals, or cerebral blood volume (CBV) and blood flow (CBF) changes, positron emission tomography (PET) measures CBF, and near infrared imaging (fNIR) measures changes in deoxygenated and total hemoglobin (Attwell et al., 2010; Logothetis, 2010). However, the mechanisms that modulate NVC are not fully understood, which in part reflects limitations of currently available imaging techniques that make it difficult to image long-term NVC dynamics at high temporal and spatial resolutions.

The investigation of the dynamic coupling between neuronal activity and changes in CBF ideally requires the capabilities to 1). Simultaneously image hemodynamic changes in neurovascular networks (e.g., CBF, CBV, and hemoglobin oxygenation) along with neuronal activity; 2). High spatial resolution to separately distinguish neuronal activity from vascular changes in arteries and veins; 3). High temporal resolution to capture stimulation-induced neuronal activation and hemodynamic responses in real-time; 4). A large field of view (FOV) to provide quantitative imaging of CBF in the neurovascular network; and (5) Capabilities for long-term measures of neuronal activity and hemodynamics, which are important to evaluate disease progression.

Conventional neuroimaging tools such as fMRI, PET and fNIR imaging have greatly advanced our understanding of brain function (Baron et al., 1982; Chance et al., 1998; Girouard and Iadecola, 2006); however, their spatial resolutions are limited (e.g., ~1mm) and insufficient to resolve individual vascular compartments or cells in vivo, although recent work in animals has begun to resolve individual vessels with fMRI (Yu et al., 2012; Yu et al., 2016). Multi-photon microscopy allows one to visualize the capillary vasculature and cellular details in the rodent cortex in vivo, but its FOV is too small to assess neuronal and vascular networks over a large cortical volume (e.g., > $1mm^3$ (Helmchen and Waters, 2002)). To date, no study has assessed neuronal activity in parallel to the associated hemodynamic responses in real time across a several millimeter FOV at single cell and

single vessel resolution. In addition, the challenges of maintaining a clear and unobstructed view of the cortex (Roe, 2007) and of long-term labeling of calcium fluorescence in a living brain makes it particularly difficult to image the cortex over a long time period (e.g., months). However, this is desirable when characterizing the progression of hemodynamic and neuronal changes in animal models of brain diseases that affect NVC. Herein, we developed an optical strategy to directly image both neuronal calcium signaling and neurovascular events to sensory stimulation with single cellular and vascular resolution in the mouse cortex longitudinally over an eight weeks period.

2. Material and Methods

All experiments were carried out according to National Institutes of Health guidelines and were approved by the Institutional Animal Care and Use Committee at Stony Brook University. C57B6 mice (Jackson) were used. All animals were housed in a 12:12 hour light-dark cycle. During the experiment, heart rate and body temperature were continuously monitored to ensure normal physiological condition of the animals.

2.1 Virus Injection and Cranial Window Implantation

Surgical procedures and AAV vector injections were performed under anesthetic conditions. At first, ketamine (10 mg/kg) and xylazine (20 mg/kg) were injected intraperitoneally (i.p.). Mice were placed in a stereotaxic apparatus under inhalational 1.5–2.5% isoflurane and their heads shaved using a small animal trimmer (Model No 41591-04302, Wahl). A small hole was created in the skull over the hindpaw (HP) cortical area using a dental drill (XL-30w, OSADA Electric), and 0.3ul of GCaMP6f virus (AAV1.Syn.GCaMP6f.WPRE.SV40, Penn Vector Core) was slowly injected into the HP cortex (AP −0.7mm, ML 1.5mm) for neuronal uptake. After the injection, animals were monitored daily to ensure that they remained healthy.

For the cranial optical window implantation, a region of interest (lateral: from 0.25 to 2.75 and anterior: from −0.25 to −2.75) was selected on the sensorimotor cortex. The cortical bone was thinned using a dental drill and was then carefully removed, leaving the dura intact. Dexamethasone sodium phosphate (50989-437-12, VEDCO) was applied to the exposed brain region that was then immediately covered with a 3×3 mm^2 sterile coverslip and sealed with biocompatible glue. Dental cement was spread around the edge of the coverslip to further secure its attachment with the skull for longitudinal studies.

2.2 Multimodal Optical Imaging

In vivo optical imaging was conducted in animals anesthetized with dexmedetomidine (i.e., DEX, Pfizer, 0.0125mg/kg, i.p.). A custom-built multimodal optical imaging platform (MIP) was used (Fig. 1A), which includes multi-wavelength spectral and fluorescence imaging and laser speckle contrast imaging (LSI) modules (MW-LSI)–integrated with three dimensional (3D) optical coherence tomography (3D OCT). In MW-LSI, 2 high-brightness light-emitting diodes (LEDs) at wavelengths of λ_1=488nm and λ_2=568nm were used for exciting GCaMP6f-expressed intracellular calcium ($[Ca^{2+}]_i$) fluorescence and total hemoglobin (HbT) imaging, respectively; a pigtailed diode laser (60mW) at λ_3=830nm was delivered

through a monomode fiber for LSI imaging. The fiber guided illumination was incident on the cortical brain through a chronic cranial window, in which the 3-channel light sources were pulse-modulated to sequentially illuminate the cortex and synchronized by a time-base interfaced with a computer for simultaneous imaging. The back-reflected light from each channel was collected through a modified zoom microscope (AZ100, Nikon) and acquired by a 16-bit sCMOS camera (Zela 4.2; Andor) at either 80 or 16 fps (Du et al., 2014).

The 3D-OCT system was integrated with MW-LSI via a dichroic mirror (i.e., DM1, Fig. 1A). Light exiting from the sample arm was connected to a custom scan head (C1) mounted on the microscope objective, in which ϕ5-mm collimated beam from the sample arm was transversely scanned by a pair of Galvo scanner (VM500; General Scanning), focused by an objective lens (f40 mm/0.1 N.A.) and reflected by DM1 onto the cortex. A typical FOV of 3 × 3 mm^2 on the cortex was imaged to register and compare with LSI. Different from optical coherence angiography (OCA) for morphological imaging of the neurovascular network, specific raster scanning schemes were implemented to optimize the flow detection sensitivity for 3D optical coherence Doppler tomography (ODT), by which the camera was configured to operate at 20,000 A-lines per second with dense sampling (e.g., 0.05-μm pitch) along the x axis for fast blood flow such as in the large vessels and down-binned to 10,000 and 5,000 A-lines per second in post image processing to enhance the slow blood flow such as in the small vessels. This imaging platform can provide multimodal images including GCaMP $[Ca^{2+}]_i$ fluorescence, HBT, CBF, OCA, ODT (Figs. 1B–F).

2.3 Sensory Hind Paw Electrical Stimulation

Two needle electrodes inserted under the skin of contralateral hind paws of the mouse were connected to an electrical stimulator (A-M System 2100, Sequim, WA, USA) and synchronized with the image acquisition. Each hindpaw stimulation epoch lasted 10s, during which a serial of 1Hz or 5Hz bipolar rectangular electrical pulses (0.3ms pulse width, 3mA peak-to-peak amplitude) were delivered.

2.4 Imaging Processing and Quantitative Analyses

2.4.1 μODT and μOCA imaging—The μODT image was reconstructed from phase subtraction method (PSM), in which the apparent Doppler flow speed $v_{z,x}$ was calculated from the measured phase shift between two successive OCT A-scans ($\Delta\phi_{x,z}$), i.e., $v_{z,x}=\lambda\Delta\phi/(4\pi nT\cos\theta)$, where x, z denote lateral and axial coordinates, n is refractive index of brain tissue, T is duration between 2 A-scans, and θ is the flow or vessel angle with respect to z axis) (Ren et al., 2012; Zhao et al., 2000). Because of intensive computation, graphic processing unit (GPU) with custom GUI programming was implemented to implement fast B-scan $v_{z,x}$ reconstruction and real-time maximum intensity projection (MIP) of 3D μODT display, as well as gradient tracking or 3D Hessian matrix method angle correction of capillary CBFv networks (You et al., 2014; You et al., 2017a). μOCA was reconstructed based on the voxel decorrelation between temporally adjacent OCT B-scans to extract speckle dynamics and thus identify vasculature from surrounding static tissue (Mahmud et al., 2013). Four B-scans at a y position were recorded, i.e., $I(x, z)|t_i$ (i=1,2,3,4), then μOCA (x, z; y), as speckle variance based angiography was calculated by

$$\mathrm{uOCA}(x,z;y)=\frac{\sqrt{\frac{1}{N}\sum_{i=1}^{N}\left(I(x,z)|_{t_i}-\frac{1}{N}\sum_{i=1}^{N}I(x,z)|_{t_i}\right)^2}}{\frac{1}{N}\sum_{i=1}^{N}I(x,z)|_{t_i}}(\mathrm{N}=4) \quad \text{(A.1)}$$

Microvascular density in mouse cortex was assessed by fill factor (FF), which was calculated from μOCA image. Frangi-Hessian filter was first used to globally calculate the vessel likeness of individual pixel of an en-face μOCA image by analyzing the eigenvalues (λ_1, λ_2, λ_3) of its Hessian matrix (Frangi et al., 1998; You et al., 2017b). The calculated Frangi-Hessian vessel-likeness map was converted to a binarized vascular image using an adaptive thresholding approach and then, a thinning operation was applied to skeletonize the microvascular network (Palàgyi and Kuba, 1998). The vascular density distribution, defined as FF was calculated as a ratio of pixels occupied by skeletonized vessels to the total pixel numbers within a ROI,

$$\mathrm{FF}=\frac{\mathrm{Total\ \ pixels\ \#\ occupied\ \ by\ \ vessels}}{\mathrm{Total\ \ pixels\ \#\ within\ \ the\ ROI}} \quad \text{(A.2)}$$

2.4.2 Cortical CBFv map—The cortical CBFv map was calculated pixel-by-pixel by processing the images in the LSI channel (λ_3=830nm). The relative CBFv change (ΔCBFv) was calculated from the speckle contrast constant $K=\sigma/\langle I\rangle$, i.e.,

$$K=\left\{\frac{\tau_C}{T}+\frac{\tau_C^2}{2T^2}\left[\exp\left(-\frac{2T}{\tau_C}\right)-1\right]\right\}^{1/2} \quad \text{(A.3)}$$

where <I> and σ denote the mean and local standard deviation of the intensity within a sub-volume, and T is the camera exposure time. CBFv defined as $\langle v^2\rangle^{1/2}$ that represents the rooted-mean-square speed of moving scattering particles (e.g., moving red blood cells in vessels) can be mapped according to the inverse proportion to the decorrelation time $\tau_c=[2\pi\alpha/\lambda\cdot\langle v^2\rangle^{1/2}]^{-1}$ of LSI and calculated by either spatial or temporal pixel binning (Boas and Dunn, 2010). To track the functional CBF response, a spatiotemporal binning strategy was developed to calculate the CBFv map (Chen et al., 2016), which was found to greatly enhance the signal-to-noise ratio and while maintaining sufficient temporal resolution for detecting single stimulation evoked cerebral hemodynamic changes.

2.4.3 Stimulation-evoked vessel diameter change—Quantification of stimulation evoked vessel diameter change in this study was retrieved from the associated blood volume changes. The images from the total hemoglobin channel at the isobetical λ_2=570nm (Fig. S1A) were found to show high vascular contrast and independent of the confounding changes in oxygenated- and deoxygenated- hemoglobin state within the vessels, thus allowing for cortical vessel segmentation at high signal-to-noise ratio. Specifically, the

vessel dilation or contraction was indicated by the marginal contrast HbT changes at vascular walls. A custom algorithm combining local adaptive vessel segmentation with distance transform was developed to generate a skeletonized vessel diameter map (Fig. S1). A local adaptive threshold method was used to segment each cortical vascular image into a binarized vessel image (Fig. S1B), which excluded potential artifacts induced by illumination and surface conditions. For each vessel, the central line and the diameter (Fig. S1C) were calculated through a distance transform algorithm, encoding the diameter value at the corresponding position in the vessel skeleton (Fig. S1D). Their changes during sensory stimulation were calculated by comparing the time-lapse vessel diameter maps.

2.4.4 Correction of tissue absorption on fluorescence detection—Because of neurovascular coupling, regional elevated neuronal activity usually is accompanied with functional hyperemia, evoking an increase in blood volume or total hemoglobin. The increase of local total hemoglobin resulted in an increase of tissue absorption that attenuated the GCaMP fluorescence emission at λ_{em}=510nm. To minimize the effect of tissue absorption on the fluorescence signal, we used an empirical correction approach. Briefly, as the wavelength of λ_2=568nm for the reflection image channel is close to that of λ_{em}=510nm for the fluorescence emission channel (i.e., <60nm), the optical pathlength difference between these two wavelengths is approximately negligible, and thereby the correction can be made by simply dividing the fluorescence ratio (i.e., $\Delta F/F_o$) by the change in the reflectance intensity over its baseline value at λ_2=568 nm (i.e., $\Delta I(\lambda_2)/I_o$),

$$\frac{\Delta F(t)}{F(t_0)} = \frac{\Delta F(t)_{\text{measure}}}{F(t_0)_{\text{measure}}} / \frac{\Delta I(t,\lambda)}{I(t_0,\lambda)} \quad \text{(A.4)}$$

2.5 Immunohistochemistry

At the cessation of *in vivo* experiment, the mouse was transcardially perfused with 0.1M phosphate-buffered saline (PBS), followed by fixation with 4% paraformaldehyde (PFA) in 0.1M PBS. After 24-hour incubation in 4% PFA, the brain was cryoprotected by immersion in a 30% sucrose solution in 0.1M PBS and sectioned to 50um-thick slices. For immunostaining of the mouse that received AAV1-Syn-GCaMP6f injection, tissue sections were treated with the primary antibody chicken anti-GFP (1:500; Life Technologies) to enhance the innate GCaMP fluorescence to facilitate: 1) identification of cellular uptake of GCaMP6f in neurons by co-staining with NeuN as shown in Fig. 2D (and Supplemental Figs. S2A–C) but not in astrocytes by co-labeling with GFAP (Figs. S2D–F), and 2) identification of subcellular GCaMP6f expression (e.g. uptake in nucleus, Figs. S2G–I). Specifically, sections with GCaMP6f GFP fluorescence were counterstained either with mouse anti-NeuN (1:500; Millipore MAB377) or rabbit anti-GFAP (1:500; Agilent) followed by their respective secondary antibodies (Alexa fluor 488 anti-chicken; Alex fluor 594 anti-mouse; Alexa fluor 594 anti-rabbit; 1:1000; Jackson ImmunoResearch). Some brain sections were stained with DAPI to assess whether GCaMP6f was expressed in the nucleus of neurons. Ex vivo Images were acquired by a Nikon Eclipses 80i fluorescence microscope or a Zeiss LSM 510 Meta confocal Microscope under 10× or 20× magnification.

2.6 Statistical Analysis

Results were reported as mean ± standard error (SEM). One-way repeated analyses of variance (ANOVA) were used to test the significant change ($p<0.05$) in the image signals within the experimental group (e.g., from week 1 to week 8), including stimulation-induced $[Ca^{2+}]_i$ and hemodynamic responses. Pairwise comparisons were then performed using paired t-test to find whether there was significant difference between different time points. For the comparison between two different experimental groups, two-tailed t-test was used to test for significance ($p<0.05$).

3. Results

3.1 Multi-modal optical imaging to access neuronal activity with changes in neurovascular network simultaneously

To image NVC, we used a custom-built optical fluorescence imaging (OFI) platform (Fig. 1A), which can provide multi-channel images of cortex from a living animal, including GCaMP $[Ca^{2+}]_I$ fluorescence, total hemoglobin or blood volume (HBT), blood flow velocity (CBFv) within cerebral tissue, along with images of vascular morphology (OCA) and quantitative CBFv (ODT) within the neurovascular network as shown in Figs. 1B–F.

Fig. 1G shows the experimental protocol. Viruses containing Synapsin-GCaMP6f (AAV1.Syn.GCaMP6f.WPRE.SV40, Penn Vector Core) as a genetically-encoded $[Ca^{2+}]_I$ fluorescence indicator were injected into the hind paw (HP) area of the somatosensory cortex (Fig. 2) in each animal to label neurons. Mice were repeatedly imaged over 8 weeks through the cranial window with a typical field of view (FOV) of ~3×3 mm^2 (Fig. 1F). For each animal, 3D OCT imaging was conducted from the first to fourth week after viral-injection to monitor the effects of the micro-injection on the neurovascular network. MW-LSI imaging was conducted from the first to the eighth week after viral-injection to image neuronal $[Ca^{2+}]_i$ signals at rest as well as $[Ca^{2+}]_i$ response along with hemodynamic changes induced by electrical hind-paw stimulation.

3.2 GCaMP6f neuronal expression and imaging *in vivo*

As illustrated in Fig. 2A, 1 day after AAV injection we carefully removed the bone over the HP somatosensory cortex and mounted a cover glass secured with dental cement. Blood vessels were clearly visible through the cranial window and visibility did not change over the 8-week period of the experiment (Figs. S3A1, S3A2, S3A2), indicating that this animal model with GCaMP injection approach was suitable for longitudinal imaging. Figs. 2E–L are representative cortical fluorescence images for 8 weeks, obtained from an animal injected with GCaMP6f, revealing the spatial and temporal development of GCaMP6f-labeled $[Ca^{2+}]_i$ fluorescence as a function of time. It shows that GCaMP6f $[Ca^{2+}]_i$ fluorescence was not clearly visible until the second week post injection (Figs. 2E–F). After ~20 days (i.e., by 3 weeks) post injection, strong epifluorescence signals were observed around the injection spot (e.g., pointed by an arrow in Figure 2G) that then extended peripherally into the surrounding cortical area through the 8 weeks of recording (Figs. 2H–L).

The average time course for the changes in GCaMP6f $[Ca^{2+}]_i$ fluorescence intensities were measured prior to and up to 8 weeks post viral-injection (n=6, Fig. 2M). GCaMP6f fluorescence intensity *(F)* increased from non-detectable at Day 0, to 448±11.4 (photon counts) at 1 week post injection, 1208±40.29 (photon counts) by the second week, and 2194±122.2 by the third week. From fourth to eighth week, the GCaMP6f expression spread horizontally (Figs. 2H–L) and fluorescence intensity increased gradually from 3246±105.4 to 6582±305.6 ($P<0.0001$, one-way ANOVA test, n=6).

To test the integrity of the tissue and virus expression around the injection site after long-term imaging, we perfused the mice for immunohistochemical examinations. Figs. 2B–D show a cross section of a brain slice image obtained from a representative animal after 4 weeks injection, which show that the AAV virus was mostly expressed in cortical Layers 2 to 4 (Fig. 2B). Fig. 2C is a 'zoom-in' view of Fig. 2B, demonstrating the GCaMP6f cellular uptake. Although a small needle scar is seen at the center of the injection site (asterisk, Fig. 2B), no major damage was observed in the surrounding tissue. Importantly, as shown in Fig. 2D (arrows in Fig. 2D and in Fig. S2C), GCaMP6f fluorescence co-localized well with NeuN (a marker of neurons) whereas there was no overlap with GFAP (Fig. S2F), which is a marker of glial cells. This confirmed that the in vivo cortical GCaMP6f signals (Figs. 2E–L) were of neuronal origin.

3.3 Micro-injection temporally disrupts local neurovascular network

We used ultrahigh-resolution OCA (μOCA) and ODT (μODT) to image the vascular morphology (Fig. 1B) and quantitative cerebral blood flow velocity (CBFv) in arteries, veins and capillaries (Fig. 1C). Additionally, LSI provided CBFv maps in cortical tissue, which allowed us to evaluate the effects of GCaMP6f micro-injection on the neurovascular network and on flow within the cortical tissue surrounding the injection site.

The chronic cranial window allowed us to periodically assess changes in the neurovascular network starting on the day of GCaMP6f micro-injection (day 0) to week 8 post-injection. Representative sequential μOCA, μODT and LSI cortical images are shown in Figs. 3A1–A6, 3B1–B6, 3C1–C6, respectively. The images revealed minor trauma from viral micro-infusion (< 300 μm, Figs. 3A1, 3A1', 3B1, 3B1' and Supplemental Fig. S3B). GCaMP6f viral injection locally damaged small vessels (circled in Fig. 3A1, Fig. S3B), interrupting blood flow (circled in Fig. 3B1) and reducing perfusion in the tissue near the injection site (circled in Fig. 3C1). Notice for example the broken vessels in the injection spot, (yellow and blue arrows in Fig. 3A2), where no detectable blood flow was observed with uODT ('black' hole as circled in Figs. 3B1, 3B1'). However, after ~3 days, blood flow in the local tissue had improved (Fig. 3C2), and a new vessel was observed in the injection site one week after viral injection (circled in Figs. 3A3, 3B3), indicative of local revascularization (Figs. 3A4–A6). Meanwhile, local CBF recovered (Figs. 3B4–B6 and Figs. 3C4–C6). Figs. 3A1', 3A6' are 'Zoomed-in' revascularization images of the neurovascular network at the injection site obtained on the first day post-injection (Fig. 3A1) and at 4 weeks post injection (Fig. 3A6), respectively. Figs. 3B1', 3B6' are corresponding CBFv images, indicating that revascularization restored CBF (Fig. 3B6') to the injection site at 4 weeks post injection.

The time course for the mean intensities of μOCA, μODT and LSI signals within the injection site changed with time post-injection (Fig. 3D). To characterize the growth of the microvascular network, a fill factor (*FF*) was measured and was calculated based on μOCA images (You et al., 2017b). Fig. 3D shows that the *FF* gradually increased from 0.057±0.0005 at Week zero to 0.064±0.0024 at the first week, and then to 0.089±0.0072 by the second week. *FF* plateaued from the third to the fourth week post viral injection (0.096±0.0043, P=0.059, n=6). The rapid changes in *FF* in the first two weeks post viral injection (i.e., from Week 0 and Week 2) reflected the increases in vascular density (P<0.001, n=6) due to revascularization. In parallel CBFv measured with μODT also increased, i.e., from 0.89±0.34mm/s at Week zero, to 5.99±0.21mm/s at second week, after which it plateaued till the fourth week (i.e., 6.46±0.13mm/s) (P<0.0001, one-way ANOVA test, n=6). The perfused blood flow in tissue detected by LSI also increased from 2.8±0.17(×10^4, a.u.) at 3 days post injection (0.5week), to 6.1±0.95(×10^4, a.u.) at the second week, 6.3±0.08(×10^4, a.u.) at the third week, and 6.4±0.81(×10^4, a.u.) at the fourth week (P<0.0001, one-way ANOVA test, n=6). The increases in μODT and LSI signals reflect CBFv increases in the local vascular network and in cortical tissue. Together, the results show that angiogenesis in cortical tissue underlies the recovery from the local neurovascular damage induced by the micro-injection.

3.4 Long term imaging of spontaneous neuronal Ca^{2+} activity and its response to sensory stimulation

By the third week post injection, spontaneous neuronal $[Ca^{2+}]_i$ activity in the resting state in cortical tissue was observed (Supplemental Fig. S4B). The relative changes of spontaneous $[Ca^{2+}]_i$ fluorescence ΔF_s over the background fluorescence F ($\Delta F_s/F$) were tracked for several weeks. Supplemental Fig. S4 shows the time course of GCaMP6f fluorescence at resting state from the third till the eighth week post injection, which indicates that the spontaneous $[Ca^{2+}]_i$ transients were detectable on the third week (Supplemental Fig. S4C) and became more robust at 3.5–4.5 weeks but then declined by the sixth to eighth weeks (P<0.0001, n=6). Specifically, mean cortical $\Delta F_s/F$ changed from ~2±0.09% at the third week, to 6.4±0.3% at the fifth week, to 4.8±0.3% at the sixth week, 3.9±0.3% at the seventh week, and 3.6±0.3% at the eighth week (P<0.0001, one-way ANOVA test, n=6), respectively. The decrease in $\Delta F_s/F$ from the sixth to eighth week could be associated with the highly expressed-G-CaMP neurons portioning into subcellular compartments such as nucleus (Supplemental Fig. S2I). It has been reported that nucleus-filled neurons developed aberrant fluorescence responses after 5 weeks of expression (Chen et al., 2013).

During the experiment, the time courses of the background fluorescence (*F*) were stable (Supplemental Fig. S4B), indicating minimal effect of cortical motion and the successful implantation of the chronic cranial window. In addition, there was no drifting observed in the $\Delta F_s/F$ traces of the ROIs for at least 5 minutes (Supplemental Fig. S4B), indicating no photo bleaching of GCaMP6f fluorescence during measurements.

To investigate the spatial and temporal profiles of neuronal populations responding to electrical HP stimulation (0.3ms, 3mA, 1Hz and duration of 10 seconds), we inserted two needle electrodes in the contralateral hind paw (HP) from the location of the cranial window.

Fig. 4A illustrates the spatial GCaMP6f fluorescence change in response to electrical HP stimulation. Fig. 4B shows typical $[Ca^{2+}]_i$ fluorescence *ΔF/F* responses to the stimulation (red dashed lines). Fig. 4D shows the 3D fluorescence intensity distribution of a $[Ca^{2+}]_i$ transient evoked by stimuli, demonstrating the larger spatial response in the cortex at 3.5–4.5 weeks post GCaMP6f injection. The response of the GCaMP6f $[Ca^{2+}]_i$ transient was synchronized with each single stimulus (Fig. 5B and Supplemental Movie M1) demonstrating the high sensitivity of GCaMP6f labeling for capturing dynamic intracellular Ca^{2+} changes (ΔF/F) in response to a single stimulation.

The mean amplitude of the stimulation-evoked fluorescence intensity change (*ΔF/F*) (Fig. 4C, n=6) was 1.5±0.08% on the third week and increased to a maximum of 6.0±0.3% at the fourth ~fifth week, then decreased to 3.1±0.4% by the eighth week ($P<0.0001$, one-way ANOVA test, n=6). Fig. 4E illustrates the single stimulation-induced spatial and temporal *ΔF/F* changes within the imaging FOV of the HP cortex. It indicates that, after the onset of the stimulus the *ΔF/F* was increased spatially in HP cortex within 0.125s and reached a peak by 0.375s. Afterwards, it declined and returned to the baseline by 0.625s, thus indicating the sensitivity of our imaging system that enables the detection of a single ΔF/F transient in response to a single electrical stimulus from hindpaw. Fig. 4F shows the superposed individual $[Ca^{2+}]_i$ transients in response to 1 Hz stimulation (3mA, 10 sec) and their average time trace (blue curve, m=20) obtained from animals (n=20 trials) after four and half weeks of G-CaMP6f injection. It indicates that the time-to-peak, duration (measured as Full-Width-Half-Maximum, FWHM), and peak amplitude of the ΔF/F transients were 368±36.6ms, 537±34ms, and 6.00±0.3%, respectively. Fig. 4G shows the *ΔF/F* changes of different ROIs across the HP cortical area, including ones located outside (ROIs ***a*** and ***f***) and within the fluorescence expression area (ROIs b–e) (Fig. 4F). The stimulation-evoked *ΔF/F* response was clearly seen within the GCaMP6f expression area, showing the ability of our protocol to identify the cortical regions that are responsive to stimulation (e.g., the circle approximately as shown in Fig. 4G).

3.5 Simultaneous multi-channel imaging of neuronal and vascular responses to stimulation

In order to investigate the NVC that occurs during brain activation we used the optical imaging platform to simultaneously image GCaMP6f $[Ca^{2+}]_i$ fluorescence (ΔF/F), total hemoglobin or blood volume (HbT) and CBFv responses to HP stimulation. In the early stage after viral injection, insufficient neuronal expression GCaMP6f through viral delivery could result in weak neuronal $[Ca^{2+}]_i$ fluorescence and hemodynamic responses to 1Hz stimulation. Therefore, a strong stimulation paradigm (e.g., 3mA, 5Hz, 10s) was used to generate a robust neuronal and hemodynamic reaction to ensure that neuronal and hemodynamic changes (e.g., $[Ca^{2+}]_I$, HBT, CBFv) at the early time points after injection could be detected. These longer, higher frequency stimulations have been used for fMRI studies of rodent somatosensory cortex.

Figs. 5A–C show representative images of GCaMP6f $[Ca^{2+}]_i$ fluorescence, HbT, and CBFv in the somatosensory cortex 4 weeks after GCaMP6f expression. Figs. 5A1–A5 show the stimulation-evoked (3mA, 5Hz, 10s) $[Ca^{2+}]_i$ fluorescence changes (i.e., *ΔF/F*) in spatial

domain. Figs. 5B1–B5 and Figs. 5C1–C5 are the dynamic changes in HbT (*ΔHbT*) and CBF (*ΔCBFv*) in response to HP stimulation, respectively. The neuronal $[Ca^{2+}]_i$ fluorescence *ΔF/F* increased immediately (i.e., t< 1.8s, Fig. A2) in response to the HP stimulation (i.e., started at t_0= 5 sec as shown in Fig. 5D) and peaked at ~5.8 sec after stimulation (Fig. 5A3). Meanwhile, the regional hemodynamic responses (*ΔHbT* and *ΔCBFv*) were increased and peaked correspondingly (Fig. 5B3 and Fig. 5C3). Fig. 5D shows the time courses for the average changes in *ΔF/F, ΔHbT* and *ΔCBFv* in response to stimulation across animals (n=6). Unlike the *ΔF/F* changes in response to 1Hz stimulation (shown in Fig. 4B previously), 5Hz stimulation was too fast to get individual *ΔF/F* transients. The mean duration of single *ΔF/F* transient from for GCaMP6f is ~ 540ms as measured with 1Hz stimulation. The time interval between pulses at 5Hz stimulation is only 200ms, which is too short to permit the *ΔF/F* signal to be fully recovered. This fast stimulation induced neuronal mean $[Ca^{2+}]_i$ to be raised and resulted in an increase in in mean *ΔF/F* fluorescence (Fig. 5D).

Sensory stimulation induced a 5.6±0.05% increase in neuronal $[Ca^{2+}]_i$ fluorescence (*ΔF/F*) during 5Hz stimulation. Concurrently, *ΔHbT* increased 3.2±0.07%, and *ΔCBFv* increased 44±2%. Interestingly, ΔHbT and ΔCBFv started to decrease before the stimulation period ended, whereas neuronal Ca^{2+} fluorescence persisted. *ΔHbT* and *ΔCBFv* returned to baseline 4–5 seconds after the end of the HP stimulation whereas neuronal Ca^{2+} fluorescence returned to baseline only after 9–10 seconds. Similarly, others have also observed that for prolonged stimulation (e.g., ≥ 10 sec) *ΔHbT* tended to return to baseline after the initial peak at ~ 6s, which might reflect constriction of pial arteries in the cortical surface (Devor et al., 2008; Hillman, 2014). The post-stimulus arterial vasoconstriction could play a role in the post-stimulus undershoot as observed by fMRI (Buxton, 2012). These results demonstrate that our multi-modal imaging platform can distinguish neuronal activity changes and hemodynamic responses to stimulation simultaneously in the living brain. However, it is clear that a higher frequency, longer-term stimulation leads to effects that are different and likely not a sum of individual slower frequency responses, including the early vasoconstriction and the very prolonged recovery of calcium in this case.

The HP stimulation experiment was repeated weekly and *ΔF/F, ΔHbT, ΔCBFv* signals were recorded over 8 weeks. The stimulation-evoked hemodynamic responses of *ΔHbT, ΔCBFv* were detectable in the first and second week post injection but were relatively weak (i.e., *ΔHbT*<4%, *ΔCBFv*<25%) (Fig. 5E), which likely reflected micro-damage at the site of injection. However, at 3 weeks post injection, the stimulation-induced hemodynamic change increased, which most likely reflected recovery of the vasculature damage (Fig. 3D). Specifically, *ΔHbT* was 2.1±0.02% in the first week and increased to 4.35±0.1% in the third week; and *ΔCBFv* was 23±2% in the first week and increased to 55±1.6% in the third week (n=6). Afterwards, the stimulation-induced hemodynamic responses stabilized, *ΔHbT* from 4.25±0.4% at fourth week to 5.1±0.27% at eighth week (P=0.094, one-way ANOVA test, n=6); and *ΔCBFv* from 58.9±5.8% to 63.3±5.1% (P=0.798, one-way ANOVA test, n=6). The amplitude of ΔF/F for sensory stimulation increased from 3.0±0.17% in the third week to reach a peak of 8.9±0.6% at ~ 4.5 weeks and then declined to 5.9±0.19% at the eighth week (P<0.0001, one-way ANOVA test n=6). These results indicate that with the chronic window neurovascular responses to stimulation can be imaged for more than 8 weeks and

that the best time-period for imaging is around the fourth or fifth week post GCaMP6f injection.

3.6 Simultaneous imaging of stimulation-induced neuronal activation and corresponding vascular dilation at neuronal and single vessel resolution

To study NVC, it would be useful to capture neuronal calcium changes in parallel to the associated hemodynamic changes across a large FOV in real time at single cell and single vessel resolution. Fig. 6 and Supplementary Fig. S5 demonstrate that our multimodal imaging system has the capability to do this from cells near the cortical surface.

Fig. S5 shows the heterogeneous responses of cortical neurons in response to HP stimulation (3mA, 5Hz, 10s). As illustrated in Fig. S5A1, the stimulation immediately evoked Ca^{2+} *ΔF/F* increase (Δt=0.1s, i.e., at t~5s) in the HP cortex (i.e., 'original response area' marked as a white dished area in Fig. S5A1), indicating neuronal activation induced by the sensory stimulation. Interestingly, the activation rapidly extended over the surrounding area within seconds (Fig. S5A2), and shifted to an anterior-lateral (A–L) direction toward the forepaw (FP, 'secondary response area') cortex at t=7s (Fig. S5A3). At t=8–9 seconds the intensity of *ΔF/F* signals was decreased in the HP area but the activation in the FP cortex was still detectable (Fig. S5A5). This demonstrates the capability of our optical image to capture the activity of a neuronal population within a relatively large FOV, which allowed us to track the 'cross-talk' of neuronal activation from HP to FP cortex for this long and intense stimulation paradigm (for detail dynamic changes, see Movie M2).

The 'zoomed-in' pictures of Figs. 6A1–A3 in Panel A (Fig. 6) show single neuron with GCaMP6f expression obtained 4 weeks post G-CaMP6f injection. For example, the green dots in Panel A, or white spots in grey images A1–A3 are G-CaMP6f enhanced neurons. Several neurons, e.g., cell 1 to cell 6 in Figs. 6A1–A3 were selected to demonstrate their activities during the resting state (Fig. 6D) and their responses to HP stimulation (3mA, 5Hz, 10s). The cells were estimated to be ~250μm below the cortical surface (e.g., Fig. 2B). Fig. 6D shows spontaneous calcium transients of individual neurons, i.e., cell 1 to cell 6 at resting state, indicating the high sensitivity of our imaging system to image neuronal activity at single cell resolution. Fig. 6B shows two-dimensional (2D) projection of the total hemoglobin image obtained from the HbT channel (λ=570 nm) simultaneously with the fluorescence channel, demonstrating the capability to image the neurovascular network at single vessel resolution.

To analyze NVC at the single neuron and single vessel scale we chose 3 different ROIs along the direction from HP to FP, i.e., A1, A2, A3 in HP, region between HP and FP (the so-called boundary B), and FP areas (Panel A, Fig. 6). In each ROI, two neurons (e.g., cell 1 and cell 2 in A1) and two micro vessels in the same area (diameter <50um as shown in Panel B, e.g., V1 and V2 in Panel C, Fig. 6) were selected to track the stimulation-induced changes in $[Ca^{2+}]_i$ fluorescence (*ΔF/F*) and in micro vessel dilations ($\Delta\phi/\phi$) (Panel C, Fig. 6). Fig. 6E shows the time traces of $[Ca^{2+}]_i$ ΔF/F signals of cells 1–6 (color lines) superposed with the corresponding near-by micro vessel dilations (black dashed curves). It shows that, cells 1 and 2 responded first, i.e., immediately following stimulation and peaked at t_p ~1.5–2.5s, then cells 3–4 followed (t_p ~3s–4.2s) and finally cells 5 and 6 (t_p~5s–6s)

(Supplemental Movie M3). The vascular responses followed the neuronal activation (Supplemental Movie M4) but with a consistent ~ 2 seconds delay from the $[Ca^{2+}]_i$ *ΔF/F* signal (Fig. 6F). Fig. 6G shows the temporal correlation between the local neuron activities and the vascular responses to the stimulation, indicating a high coupling between them (correlation coefficient, R= 0.978). These results demonstrate the capability of our imaging system to monitor stimulation-evoked neuronal and hemodynamic changes at high spatial (single neuron and single micro vessel < 50um, diameters) resolution and high temporal resolution (millisecond level). Supplemental Figs. S5B–D illustrate the $[Ca^{2+}]_i$ fluorescence changes in HP, Boundary and FP cortical regions in response to HP stimulation observed from different animals. The time to peak of *ΔF/F* response in HP, Boundary, FP cortical area were 2.54±0.31s, 4.8±0.28s, 6.9±0.18s, respectively (n=3).

4. Discussion and Conclusions

In this study, we report on an *in vivo* optical imaging platform that can be combined with genetically encoded calcium indicator and a cranial chronic window over the somatosensory cortex to image the neurovascular network repeatedly over 8 weeks at single neuron and single vessel resolution in a relatively large FOV. These capabilities allowed detection of spontaneous neuronal activity during the resting state and to measure the dynamic neuronal and hemodynamic responses to sensory HP stimulation longitudinally. This allowed us to characterize the recovery of the neuronal tissue to the local injury from viral injection and to monitor the changes in the strength of the $[Ca^{2+}]_i$ fluorescence signal as a function of time from injection.

Our studies demonstrate that:

1. The single stimulation-evoked GCaMP6f $[Ca^{2+}]_i$ signal, measured by using *ΔF/F* fluorescence change in response to sensory stimulation, were detectable at the 3rd week post GCaMP6f delivery with peak intensities observed during the fourth - fifth week (Figs. 4B–C). *ΔF/F* $[Ca^{2+}]_i$ fluorescence slightly declined after the fifth week possibly due to subcellular accumulation of GCaMP6f such as in the neuron's nucleus (Chen et al., 2013). Nonetheless, the *ΔF/F* signal in response to sensory stimulation was still robust and over 4% at the eighth week (Fig. 4C). This indicates the capability of this technique for long-term tracking of neuronal Ca^{2+} responses to single stimulation.
2. The *ΔF/F* $[Ca^{2+}]_i$ fluorescence and hemodynamic changes (*ΔHbT* and *ΔCBFv*) in the cortex were simultaneously imaged from the third to the eighth week post viral delivery (Fig. 5), thus indicating that our multi-modality imaging allows for longitudinal studies of NVC.
3. A large population of neurons (e.g., ~ >200 neurons in Fig. S5 or Supplemental movie M3) were observed within the FOV of the image during 5Hz, 10s stimulation. The activation of these neurons with their surrounding vessels were simultaneously recorded in response to sensory HP stimulation. The neurons in the HP cortex were immediately activated and then extended to the surrounding cortical area (Supplemental Fig. S5). Contiguous micro-vessels were dilated in

response to the stimulation following activation of neurons (Fig. 6E), but with a ~ 2 s delay to the neuronal responses (Fig. 6F). Moreover, the temporal responses between the neurons and vessels were highly correlated (R=0.98, Fig. 6G). This observation was reproducible (Fig. 6H); however, the responses to the high-frequency and long stimulation were likely not simply a sum of stimulations. For example, vasoconstriction occurred before the stimulation ended and the spread to surrounding areas was not expected.

4. The micro-injection for GCaMP delivery induced minor damage (≤ 300μm) in the local neurovascular network (Fig. S3), but it recovered (< 2 weeks) as angiogenesis (Fig. 3A6') progressively restored CBF in the injection site (Fig. 3B6').

The longitudinal imaging approach developed here is important because neuropathology for many of the brain diseases emerges progressively (Hamilton et al., 2010) and thus animal models would benefit from the capability to monitor the progression of those changes in vivo. Moreover, the disruption of hemodynamic processes has been implicated in many brain diseases such as stroke, Alzheimer's disease, diabetes, and drug abuse and its implicated in the cognitive and behavioral deterioration associated with aging (Hillman, 2014). Thus, an imaging method that allows the study of dynamic interactions of neurons with their surrounding neurovascular networks longitudinally is a powerful tool to explore the mechanism of diseases in the relevant animal models and will also be of value for assessing responses to treatment.

Calcium changes are involved in many cellular processes including neuronal plasticity and excitability (Helmchen et al., 1999). In excitable cells, calcium fluxes are closely linked to electrical activity (Helmchen and Waters, 2002). Thus, measurements of cellular calcium changes reflect neuronal activation. The genetically encoded Ca^{2+} indicator offers cell-specific targeting and longitudinal assessment. Genetically encoded calcium indicators (GECIs) have been successfully used to record stimulation-induced responses in the somatosensory and visual cortices of mice through chronic windows using microscopic imaging (Andermann et al., 2011; Grienberger and Konnerth, 2012; Minderer et al., 2012). However, microscopic imaging has a small FOV limiting the assessment to restricted areas and also requires the intravenous infusion of a fluorescence contrast agent in order to image CBF (Rosenegger et al., 2015). Direct measure of neuronal activity requires voltage sensitive indicators and a new generation of genetically encoded indicators are emerging and can be incorporated (Lou et al., 2016).

When we stimulated at 3mA, 5Hz for 10 seconds we observed that the stimulation-evoked calcium signaling extended from HP into FP cortex. This likely reflects neuronal connectivity between the nearby cortical regions but can propagate via thalamocortical interactions as well. However, this stimulation-evoked spreading of $[Ca^{2+}]_i$ activity beyond the HP observed here is different from the slow Ca^{2+} oscillations previously reported by others (Kerr et al., 2005, Steriade, 2006, Stroh et al., 2013). Firstly, the Ca^{2+} signal observed here increased rapidly in response to stimulation and gradually recovered after stimulation, thus indicating stimulation-evoked origin. In contrast, the Ca^{2+} oscillation waves changed periodically going up-to-down at each location while it spread continuously to the

surrounding cortical areas. Secondly, in our study the transfer speed of the response from HP to FP was ~0.5– 1mm/s during the stimulation period, while the Ca^{2+} oscillation wave previously reported was faster (e.g., >30mm/s;(Stroh et al., 2013). In addition, the Ca^{2+} indicator and the anesthesia used in prior studies were different from those used here.

The observation of spread of Ca^{2+} responses is also distinct from cortical spreading depression (CSD)which has a much slower wave propagation (i.e., ~ 3–5mm/min). CSD also completely depolarizes brain cells for about 1 min followed by silencing of brain electrical activity that lasts several minutes (Dreier, 2011; Enger et al., 2015; Pietrobon and Moskowitz, 2014; Somjen, 2001). Indeed, as shown in Fig. 5D and Fig. 6E, our results showed that the $Ca^{2+}{}_i$ signals induced by the stimulation paradigm of (3mA, 5Hz, 10s) returned to baseline shortly after the stimulation (< 10 seconds) and spontaneous neuronal activity was observed after stimulation (e.g., t > 25s, Supplemental M3). fMRI experiments have also detected activation into neighboring regions (Goloshevsky et al., 2011) during somatosensory stimulation and voltage-sensitive dye imaging has detected crosstalk between sensory areas (Grinvald and Hildesheim, 2004). The mechanism underlying the cross talk between HP and FP after stimulation is unclear, but could be associated with horizontal axonal connection (Kerr et al., 2005; Steriade, 2006) and/or intracortical fibers between cortical areas (Gonzalez-Burgos et al., 2000; Telfeian and Connors, 2003). There is also sufficient time for thalamocortical interactions to influence the spreading.

However, care should be taken in interpreting the results from the faster, longer stimulation. An intensive stimulation paradigm such as 5Hz over 10s results in a nonlinear neuronal and hemodynamic response in brain (Schulz et al., 2012), as clearly measured by the vasoconstriction that occurred prior to the stimulation stopping and the very slow recovery of the GCAMp6f fluorescence.

A limitation of our study was that imaging was restricted to the brain surface except for the OCT imaging. Unlike 2-photon or confocal microscopy (Chelaru and Dragoi, 2014; Fiscella et al., 2015), the surface reflection approach of fluorescence imaging applied to highly scattering tissue such as brain does not enable to reject scattering noise from out-of-focal-plane of brain tissue. Therefore, the detected Ca^{2+} fluorescence intensity could be an integration of Ca^{2+} from a selected single neuron and the background Ca^{2+} florescence. In other words, the Ca^{2+} fluorescence intensity from the selected cellular ROI could be partially attributed to that of the surrounding neuronal populations. Deeper cortical imaging should be possible with a slight modification of the light source and detection for longer wavelengths in combination with GECIs, which emit at the near infrared region (Akerboom et al., 2013; Inoue et al., 2015). Furthermore, alternative techniques such as spatially restricting neuronal cell types and spatial expression from a transgene places in a relevant endogenous locus would be useful for achieving higher specificity, higher expression, and avoiding damage and possibly enable imaging for longer times (Sadakane et al., 2015).

Our ultrahigh-resolution OCT technique provides uOCA and uODT simultaneously, which permits imaging the morphology of the neurovascular network and quantifies the CBF within the vessels including the microcirculation in capillaries (You et al., 2015). In this study, we observed revascularization around the first week and recovery of CBF at the

second week post GCaMP delivery. Interestingly, other studies have shown that revascularization was associated with neurogenesis (Carmeliet, 2003; Palmer et al., 2000). This implies that the revascularization after trauma may alleviate neuronal damage by improving local CBF and metabolite delivery to the nutrient-deprived neurons (Frontczak-Baniewicz and Walski, 2003). However, whether the accelerated revascularization in mice brains would aid the axonal remodeling or neural integrity deserves further investigation, which can be accomplished using our multi-modal system.

In the early stage following viral injection, there was insufficient neuronal GCaMP expression and injection-induced damage to microvessels that resulted in weak signals from both neuronal Ca^{2+} fluorescence and hemodynamic responses to the stimulation. A strong stimulation paradigm (3mA, 5Hz and 10s) was chosen to ensure that neuronal and hemodynamic signals (e.g., Ca^{2+}, HBT, CBFv) were detectable. To keep consistency over the repeated measurements for several weeks, the same stimulation paradigm was applied throughout the study. With this stimulation paradigm, we have observed a long-tail recovery in Ca^{2+} fluorescence signal (e.g., ~9–10s after stimulation) that was longer than the hemodynamic response (Fig. 5D). This is likely due to dysregulation of Ca^{2+} from the long stimulation in combination with the GCaMP6f buffering properties (Schulz et al., 2012).

Our study was conducted on anesthetized animals using dexmedetomidine (DEX) Dexmedetomidine is a α2-adrenergic receptor agonist (Montijn et al., 2016). Unlike many other anesthetics (e.g., volatile anesthetics such as isoflurane, etc.) that deeply suppress central nervous system (CNS) activity (Rehberg et al., 1996), DEX induces a neural state similar to natural sleep (Nelson et al., 2003). This anesthetic method has been widely used in fMRI studies. We chose this drug based on its following advantages for brain function studies, including that it can provide 1) long-term stable physiological conditions (>2hrs) (Pawela et al., 2009; Weber et al., 2006); 2) reproducible BOLD responses to FP stimulations that are similar to those of α-chloralose, which preserves brain activity and neurovascular coupling (Keilholz et al., 2004); 3) preserves frequency dependent stimulation BOLD responses and the strength of resting state functional connectivity (Jelescu et al., 2014; Magnuson et al., 2014; Pawela et al., 2009)

In summary, the techniques presented here remove an obstacle for studying NVC over a long period of time. In future studies, the technique, combined with an awake animal model and various cognitive tasks, should shed light on the organization and plasticity of the NVC.

Supplementary Material

Refer to Web version on PubMed Central for supplementary material.

Acknowledgments

We thank K. Park for assisting with animal handling, Kevin Clare and Angela Chen for the help on staining. This research was supported in part by Grant 2013CB733801 from the National Basic Research Program of China (X. G.), also by National Institutes of Health grants R01DA029718 (C.D., Y.P.), R21DA042597 (Y.P., C.D.), and R01-NS084817 (C.D).

References

Akerboom J, Carreras Calderon N, Tian L, Wabnig S, Prigge M, Tolo J, Gordus A, Orger MB, Severi KE, Macklin JJ, Patel R, Pulver SR, Wardill TJ, Fischer E, Schuler C, Chen TW, Sarkisyan KS, Marvin JS, Bargmann CI, Kim DS, Kugler S, Lagnado L, Hegemann P, Gottschalk A, Schreiter ER, Looger LL. Genetically encoded calcium indicators for multi-color neural activity imaging and combination with optogenetics. Front Mol Neurosci. 2013; 6:2. [PubMed: 23459413]

Andermann ML, Kerlin AM, Roumis DK, Glickfeld LL, Reid RC. Functional specialization of mouse higher visual cortical areas. Neuron. 2011; 72:1025–1039. [PubMed: 22196337]

Attwell D, Buchan AM, Charpak S, Lauritzen M, Macvicar BA, Newman EA. Glial and neuronal control of brain blood flow. Nature. 2010; 468:232–243. [PubMed: 21068832]

Baron JC, Lebrun-Grandie P, Collard P, Crouzel C, Mestelan G, Bousser MG. Noninvasive measurement of blood flow, oxygen consumption, and glucose utilization in the same brain regions in man by positron emission tomography: concise communication. J Nucl Med. 1982; 23:391–399. [PubMed: 6978932]

Boas DA, Dunn AK. Laser speckle contrast imaging in biomedical optics. Journal of Biomedical Optics. 2010; 15 011109-011109-011112.

Buxton RB. Dynamic models of BOLD contrast. Neuroimage. 2012; 62:953–961. [PubMed: 22245339]

Carmeliet P. Blood vessels and nerves: common signals, pathways and diseases. Nat Rev Genet. 2003; 4:710–720. [PubMed: 12951572]

Chance B, Anday E, Nioka S, Zhou S, Hong L, Worden K, Li C, Murray T, Ovetsky Y, Pidikiti D, Thomas R. A novel method for fast imaging of brain function, non-invasively, with light. Opt Express. 1998; 2:411–423. [PubMed: 19381209]

Chelaru MI, Dragoi V. Negative correlations in visual cortical networks. Cerebral Cortex. 2014; 26:246–256. [PubMed: 25217468]

Chen TW, Wardill TJ, Sun Y, Pulver SR, Renninger SL, Baohan A, Schreiter ER, Kerr RA, Orger MB, Jayaraman V, Looger LL, Svoboda K, Kim DS. Ultrasensitive fluorescent proteins for imaging neuronal activity. Nature. 2013; 499:295–300. [PubMed: 23868258]

Chen W, Park K, Volkow N, Pan Y, Du C. Cocaine-Induced Abnormal Cerebral Hemodynamic Responses to Forepaw Stimulation Assessed by Integrated Multi-wavelength Spectroimaging and Laser Speckle Contrast Imaging. IEEE J Sel Top Quantum Electron. 2016; 22:1–1.

Devor A, Hillman EM, Tian P, Waeber C, Teng IC, Ruvinskaya L, Shalinsky MH, Zhu H, Haslinger RH, Narayanan SN, Ulbert I, Dunn AK, Lo EH, Rosen BR, Dale AM, Kleinfeld D, Boas DA. Stimulus-induced changes in blood flow and 2-deoxyglucose uptake dissociate in ipsilateral somatosensory cortex. J Neurosci. 2008; 28:14347–14357. [PubMed: 19118167]

Dreier JP. The role of spreading depression, spreading depolarization and spreading ischemia in neurological disease. Nature medicine. 2011; 17:439–447.

Du C, Volkow ND, Koretsky AP, Pan Y. Low-frequency calcium oscillations accompany deoxyhemoglobin oscillations in rat somatosensory cortex. Proc Natl Acad Sci U S A. 2014; 111:E4677–4686. [PubMed: 25313035]

Enger R, Tang W, Vindedal GF, Jensen V, Johannes Helm P, Sprengel R, Looger LL, Nagelhus EA. Dynamics of Ionic Shifts in Cortical Spreading Depression. Cereb Cortex. 2015; 25:4469–4476. [PubMed: 25840424]

Fiscella M, Franke F, Farrow K, Müller J, Roska B, da Silveira RA, Hierlemann A. Visual coding with a population of direction-selective neurons. Journal of neurophysiology. 2015; 114:2485–2499. [PubMed: 26289471]

Frangi, AF., Niessen, WJ., Vincken, KL., Viergever, MA. International Conference on Medical Image Computing and Computer-Assisted Intervention. Springer; 1998. Multiscale vessel enhancement filtering; p. 130-137.

Frontczak-Baniewicz M, Walski M. New vessel formation after surgical brain injury in the rat's cerebral cortex I. Formation of the blood vessels proximally to the surgical injury. Acta Neurobiol Exp (Wars). 2003; 63:65–75. [PubMed: 12926533]

Girouard H, Iadecola C. Neurovascular coupling in the normal brain and in hypertension, stroke, and Alzheimer disease. J Appl Physiol (1985). 2006; 100:328–335. [PubMed: 16357086]

Goloshevsky AG, Wu CW, Dodd SJ, Koretsky AP. Mapping cortical representations of the rodent forepaw and hindpaw with BOLD fMRI reveals two spatial boundaries. Neuroimage. 2011; 57:526–538. [PubMed: 21504796]

Gonzalez-Burgos G, Barrionuevo G, Lewis DA. Horizontal synaptic connections in monkey prefrontal cortex: an in vitro electrophysiological study. Cerebral Cortex. 2000; 10:82–92. [PubMed: 10639398]

Grienberger C, Konnerth A. Imaging calcium in neurons. Neuron. 2012; 73:862–885. [PubMed: 22405199]

Grinvald A, Hildesheim R. VSDI: a new era in functional imaging of cortical dynamics. Nat Rev Neurosci. 2004; 5:874–885. [PubMed: 15496865]

Hamilton NB, Attwell D, Hall CN. Pericyte-mediated regulation of capillary diameter: a component of neurovascular coupling in health and disease. Front Neuroenergetics. 2010; 2

Helmchen F, Svoboda K, Denk W, Tank DW. In vivo dendritic calcium dynamics in deep-layer cortical pyramidal neurons. Nat Neurosci. 1999; 2:989–996. [PubMed: 10526338]

Helmchen F, Waters J. Ca2+ imaging in the mammalian brain in vivo. Eur J Pharmacol. 2002; 447:119–129. [PubMed: 12151004]

Hillman EM. Coupling mechanism and significance of the BOLD signal: a status report. Annu Rev Neurosci. 2014; 37:161–181. [PubMed: 25032494]

Inoue M, Takeuchi A, Horigane S, Ohkura M, Gengyo-Ando K, Fujii H, Kamijo S, Takemoto-Kimura S, Kano M, Nakai J, Kitamura K, Bito H. Rational design of a high-affinity, fast, red calcium indicator R-CaMP2. Nat Methods. 2015; 12:64–70. [PubMed: 25419959]

Jelescu IO, Ciobanu L, Geffroy F, Marquet P, Le Bihan D. Effects of hypotonic stress and ouabain on the apparent diffusion coefficient of water at cellular and tissue levels in Aplysia. NMR in Biomedicine. 2014; 27:280–290. [PubMed: 24403001]

Keilholz SD, Silva AC, Raman M, Merkle H, Koretsky AP. Functional MRI of the rodent somatosensory pathway using multislice echo planar imaging. Magnetic Resonance in Medicine. 2004; 52:89–99. [PubMed: 15236371]

Kerr JN, Greenberg D, Helmchen F. Imaging input and output of neocortical networks in vivo. Proc Natl Acad Sci U S A. 2005; 102:14063–14068. [PubMed: 16157876]

Logothetis NK. Neurovascular Uncoupling: Much Ado about Nothing. Front Neuroenergetics. 2010; 2

Lou S, Adam Y, Weinstein EN, Williams E, Williams K, Parot V, Kavokine N, Liberles S, Madisen L, Zeng H, Cohen AE. Genetically Targeted All-Optical Electrophysiology with a Transgenic Cre-Dependent Optopatch Mouse. J Neurosci. 2016; 36:11059–11073. [PubMed: 27798186]

Magnuson ME, Thompson GJ, Pan WJ, Keilholz SD. Time - dependent effects of isoflurane and dexmedetomidine on functional connectivity, spectral characteristics, and spatial distribution of spontaneous BOLD fluctuations. NMR in Biomedicine. 2014; 27:291–303. [PubMed: 24449532]

Mahmud MS, Cadotte DW, Vuong B, Sun C, Luk TW, Mariampillai A, Yang VX. Review of speckle and phase variance optical coherence tomography to visualize microvascular networks. J Biomed Opt. 2013; 18:50901. [PubMed: 23616094]

Minderer M, Liu W, Sumanovski LT, Kugler S, Helmchen F, Margolis DJ. Chronic imaging of cortical sensory map dynamics using a genetically encoded calcium indicator. J Physiol. 2012; 590:99–107. [PubMed: 22083602]

Montijn JS, Meijer GT, Lansink CS, Pennartz CM. Population-level neural codes are robust to single-neuron variability from a multidimensional coding perspective. Cell reports. 2016; 16:2486–2498. [PubMed: 27545876]

Nelson LE, Lu J, Guo T, Saper CB, Franks NP, Maze M. The α2-adrenoceptor agonist dexmedetomidine converges on an endogenous sleep-promoting pathway to exert its sedative effects. Anesthesiology: The Journal of the American Society of Anesthesiologists. 2003; 98:428–436.

Palàgyi K, Kuba A. A 3D 6-subiteration thinning algorithm for extracting medial lines. Pattern Recognition Letters. 1998; 19:613–627.

Palmer TD, Willhoite AR, Gage FH. Vascular niche for adult hippocampal neurogenesis. J Comp Neurol. 2000; 425:479–494. [PubMed: 10975875]

Pawela CP, Biswal BB, Hudetz AG, Schulte ML, Li RP, Jones SR, Cho YR, Matloub HS, Hyde JS. A protocol for use of medetomidine anesthesia in rats for extended studies using task-induced BOLD contrast and resting-state functional connectivity. NeuroImage. 2009; 46:1137–1147. [PubMed: 19285560]

Pietrobon D, Moskowitz MA. Chaos and commotion in the wake of cortical spreading depression and spreading depolarizations. Nat Rev Neurosci. 2014; 15:379–393. [PubMed: 24857965]

Raichle ME. Behind the scenes of functional brain imaging: a historical and physiological perspective. Proc Natl Acad Sci U S A. 1998; 95:765–772. [PubMed: 9448239]

Rehberg B, Xiao Y-H, Duch DS. Central nervous system sodium channels are significantly suppressed at clinical concentrations of volatile anesthetics. The Journal of the American Society of Anesthesiologists. 1996; 84:1223–1233.

Ren H, Du C, Yuan Z, Park K, Volkow ND, Pan Y. Cocaine-induced cortical microischemia in the rodent brain: clinical implications. Mol Psychiatry. 2012; 17:1017–1025. [PubMed: 22124273]

Roe AW. Long-term optical imaging of intrinsic signals in anesthetized and awake monkeys. Appl Opt. 2007; 46:1872–1880. [PubMed: 17356633]

Rosenegger DG, Tran CH, Wamsteeker Cusulin JI, Gordon GR. Tonic Local Brain Blood Flow Control by Astrocytes Independent of Phasic Neurovascular Coupling. J Neurosci. 2015; 35:13463–13474. [PubMed: 26424891]

Sadakane O, Masamizu Y, Watakabe A, Terada S, Ohtsuka M, Takaji M, Mizukami H, Ozawa K, Kawasaki H, Matsuzaki M, Yamamori T. Long-Term Two-Photon Calcium Imaging of Neuronal Populations with Subcellular Resolution in Adult Non-human Primates. Cell Rep. 2015; 13:1989–1999. [PubMed: 26655910]

Schulz K, Sydekum E, Krueppel R, Engelbrecht CJ, Schlegel F, Schroter A, Rudin M, Helmchen F. Simultaneous BOLD fMRI and fiber-optic calcium recording in rat neocortex. Nat Methods. 2012; 9:597–602. [PubMed: 22561989]

Somjen GG. Mechanisms of spreading depression and hypoxic spreading depression-like depolarization. Physiol Rev. 2001; 81:1065–1096. [PubMed: 11427692]

Steriade M. Grouping of brain rhythms in corticothalamic systems. Neuroscience. 2006; 137:1087–1106. [PubMed: 16343791]

Stroh A, Adelsberger H, Groh A, Ruhlmann C, Fischer S, Schierloh A, Deisseroth K, Konnerth A. Making waves: initiation and propagation of corticothalamic Ca2+ waves in vivo. Neuron. 2013; 77:1136–1150. [PubMed: 23522048]

Telfeian AE, Connors BW. Widely integrative properties of layer 5 pyramidal cells support a role for processing of extralaminar synaptic inputs in rat neocortex. Neurosci Lett. 2003; 343:121–124. [PubMed: 12759179]

Weber R, Ramos-Cabrer P, Wiedermann D, van Camp N, Hoehn M. A fully noninvasive and robust experimental protocol for longitudinal fMRI studies in the rat. NeuroImage. 2006; 29:1303–1310. [PubMed: 16223588]

You J, Du C, Volkow ND, Pan Y. Optical coherence Doppler tomography for quantitative cerebral blood flow imaging. Biomed Opt Express. 2014; 5:3217–3230. [PubMed: 25401033]

You J, Li A, Du C, Pan Y. Volumetric Doppler angle correction for ultrahigh-resolution optical coherence Doppler tomography. Appl Phys Lett. 2017a; 110:011102. [PubMed: 28104922]

You J, Volkow ND, Park K, Zhang Q, Clare K, Du C, Pan Y. Cerebrovascular adaptations to cocaine-induced transient ischemic attacks in the rodent brain. JCI Insight. 2017b; 2:e90809. [PubMed: 28289715]

You J, Zhang Q, Park K, Du C, Pan Y. Quantitative imaging of microvascular blood flow networks in deep cortical layers by 1310 nm muODT. Opt Lett. 2015; 40:4293–4296. [PubMed: 26371919]

Yu X, Glen D, Wang S, Dodd S, Hirano Y, Saad Z, Reynolds R, Silva AC, Koretsky AP. Direct imaging of macrovascular and microvascular contributions to BOLD fMRI in layers IV–V of the rat whisker-barrel cortex. Neuroimage. 2012; 59:1451–1460. [PubMed: 21851857]

Yu X, He Y, Wang M, Merkle H, Dodd SJ, Silva AC, Koretsky AP. Sensory and optogenetically driven single-vessel fMRI. Nat Methods. 2016; 13:337–340. [PubMed: 26855362]

Zhao Y, Chen Z, Saxer C, Xiang S, de Boer JF, Nelson JS. Phase-resolved optical coherence tomography and optical Doppler tomography for imaging blood flow in human skin with fast scanning speed and high velocity sensitivity. Opt Lett. 2000; 25:114–116. [PubMed: 18059800]

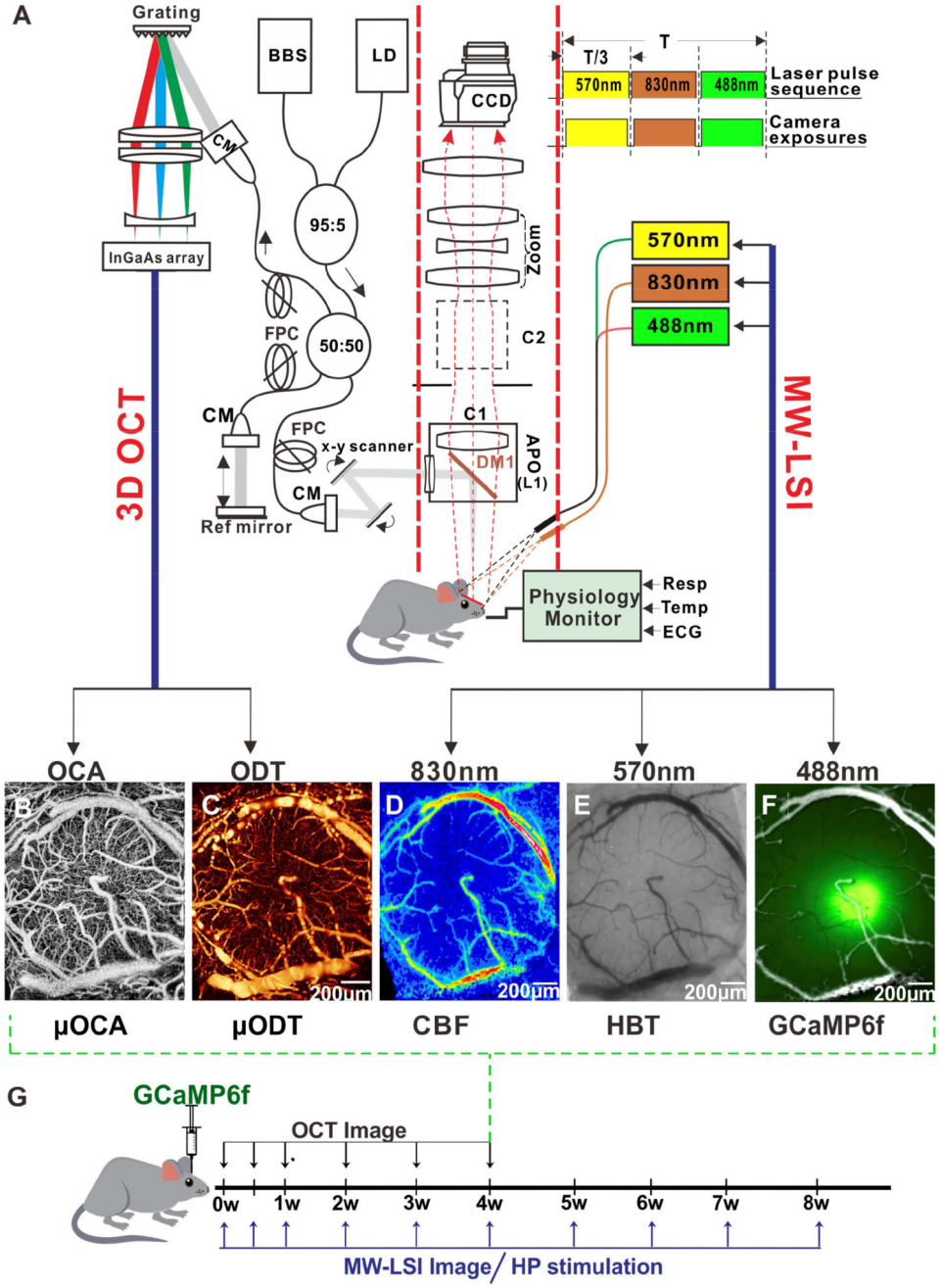

Figure 1. Schematic diagram of a multimodal optical imaging platform and imaging timeline for the study

A): The optical imaging platform combines 3D optical coherence tomography (3D OCT, left panel) and multiple wavelength laser speckle contrast imaging (MW-LSI, right panel SM: single mode; CM: collimator; BBS: broadband source; FPC: fibrotic polarization controller; C1, C2: epi-Illumination cube 1, 2. DM1: dichroic beam. splitter (λ = 1 μm); L1: 2 × APO (f =45 mm, NA = 0.22).

B, C): Representative μOCA and μODT images of the somatosensory cortex from 3D OCT, respectively.

D): Representative images by a laser diode at λ_3= 830 nm for cerebral blood flow velocity (CBFv).

E, F): Representative images obtained by using LEDs at λ_2 =570nm (**E**) and λ_1=488nm (**F**) for the total hemoglobin (HbT) and calcium fluorescence labeled by GCaMP6f.

G): Time point of the G-CaMP virus injection and imaging time line and protocol. The OCT image was taken from 0 day up to the fourth week and the MW-LSI imaging was taken from 0 day to the eighth week post GCaMP6f injection.

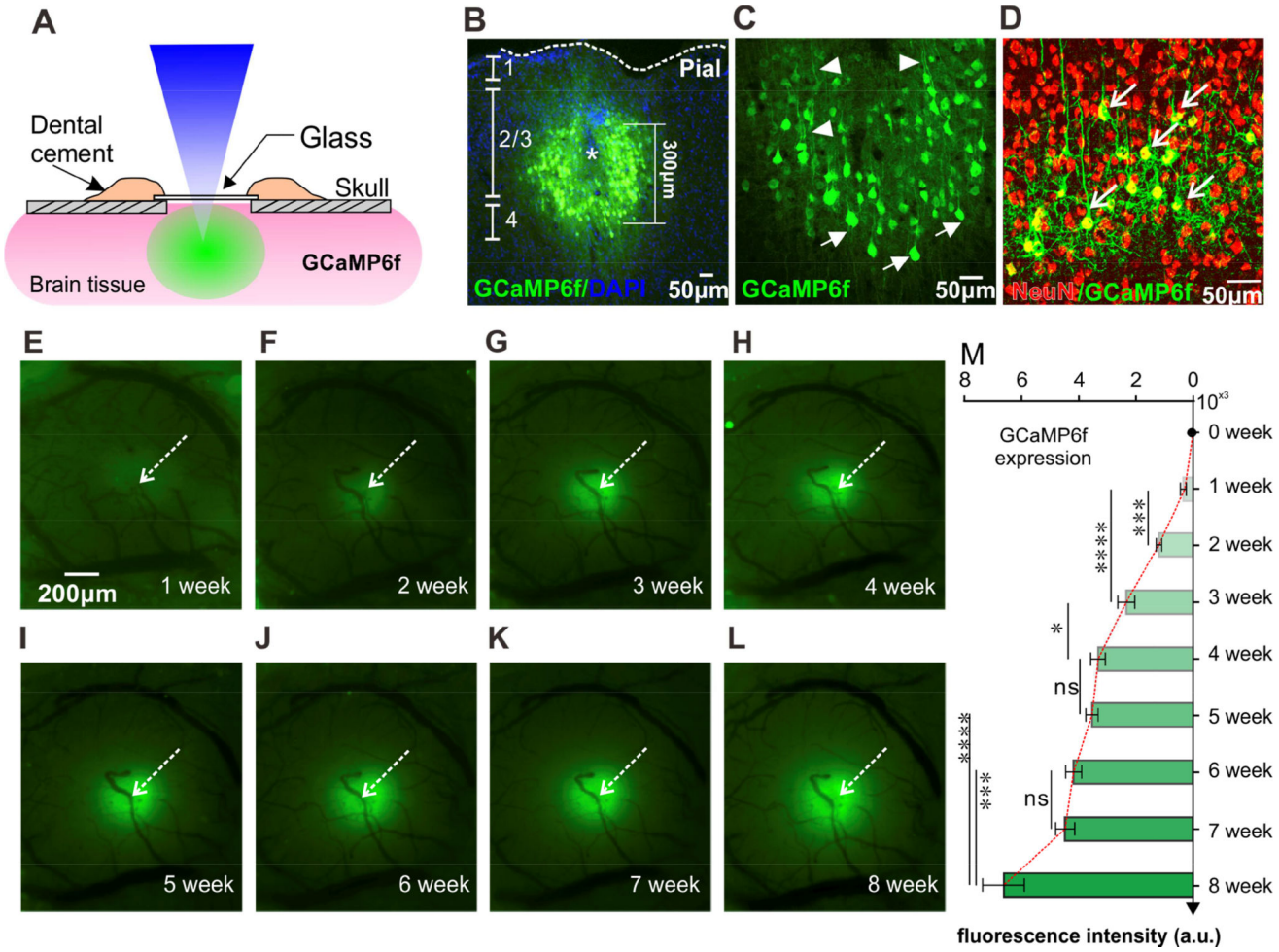

Figure 2. GCaMP6f Imaging in the sensorimotor cortex, indicating its neuronal uptake

A): Schematic illustration of the optical imaging window.

B–D): Immunohistochemical images of GCaMP6f within cortex. **B:** cross-section imaging of a brain sample, indicating GCaMP expression around the injection site within the cortex; **C:** Magnification view of G-CaMP expressing, indicating cellular uptake; **D:** GCaMP6f staining overlapping with neuronal marker NeuN, indicating GCaMP uptake specifically in neurons.

E–I): Fluorescence images obtained weekly following GCaMP virus injection, i.e., from first week to eighth week, indicating the spatial expression of GCaMP6f within the cortex.

M): Development of GCaMP6f fluorescent (*F*) as a function of time, indicating the gradual increase in *F* from the second week to the sixth week and up to the eighth week post-injection (*: $p < 0.05$; ***: $p<0.001$; ****: $p<0.0001$; ns: no significant difference. N=6). Data are mean ± SEM. See also Fig. S2 for more details

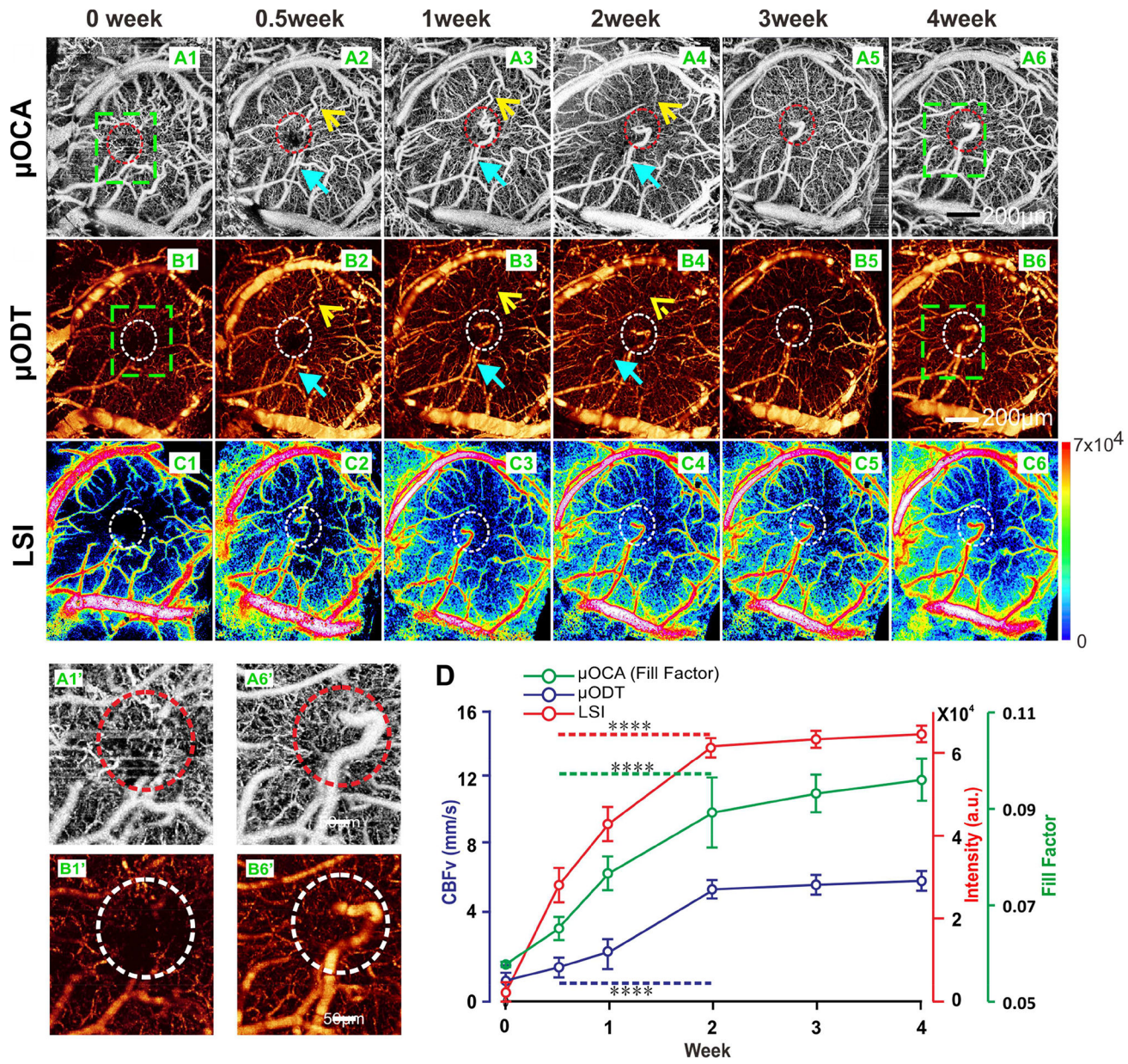

Figure 3. Revascularization after injection tracked by 3D-OCT and LSI imaging

A1–A6): μOCA image of cortex captured from day 0 (**A1**) right after injection to the fourth week (**A6**). Yellow arrows indicate the interrupted vessel due to injection; blue arrows show the new vessel. Revascularization first appeared by week 1(**A3**) after the injection, and continued until week 3.

B1–B6): μODT image captured from 0 day (**B1**) after injection to the fourth week (**B6**).

C1–C6): LSI image obtained from 0 day (**C1**) after injection to the fourth week (**C6**).

A1', B1'): Magnification view of injection site (green boxes marked in **A1, B1**) for the neurovascular angiography (**A6'**) and quantitative CBFv imaging right after injection;

A6',B6'): Magnification view of injection site (green boxes marked in **A6, B6**) for the neurovascular angiography (**A6'**) and quantitative CBFv imaging after 4 weeks, indicating that the revascularization restored CBF in the injection site.
D): Mean time courses of μOCA, μODT and CBFv signals in injection site from animals (n=6), indicating the vascular network damaged by injection fully recovered within two weeks post injection. Data are mean ± SEM. ****: $p<0.0001$.
See also Fig. S3 for more details.

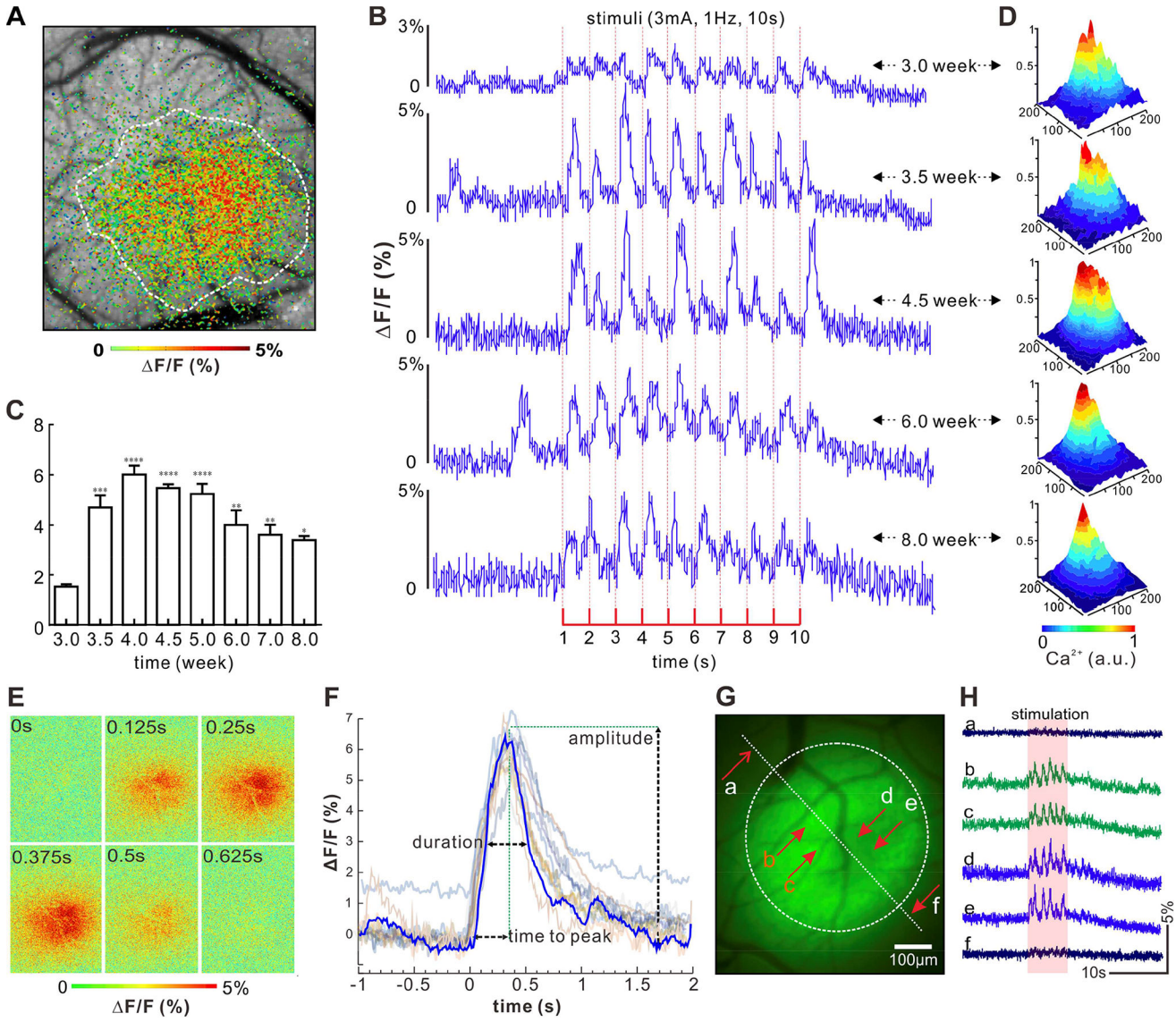

Figure 4. Spatiotemporal analysis of GCaMP6f [Ca^{2+}]i fluorescence to track activity of neuron population in cortex responding to single sensory stimulation in hindpaw (HP)

A): Demonstration of spatial response of GCaMP signal in the cortex due to HP stimulation.

B): Demonstration of GCaMP fluorescence transients in response to stimulation from the third week to the eighth week post GCaMP injection. Red dash line indicates each single stimulus.

C): Mean values of stimulation-evoked $[Ca^{2+}]_i$ transient (ΔF) over baseline (F), i.e., $\Delta F/F$ of animals (n=6) tracked from the third week to the eighth week post GCaMP injection.

D): 3D spatial fluorescence intensity increase (ΔF) in cortex induced by the HP stimulation, indicating the maximum response in area appeared~4–4.5 weeks post injection.

E): Ratio image of spatiotemporal [Ca^{2+}]i transient in response to a single stimulus, i.e., spatial view of a single transient ΔF/F on cortex obtained from the animal after 4 weeks injection;

F): Superposed individual $[Ca^{2+}]_i$ transient traces (thin lines) and their average time trace (blue curve, m=20) obtained from animals after 4.5 weeks of GCaMP6f injection. It indicates that the time-to-peak of the transient, duration (represented as Full-Width-Half-Maximum, FWHM), and peak amplitude of neuronal $[Ca^{2+}]_i$ transients are 368±36.6ms, 537±34ms, and 6.00±0.3%, respectively.

G): Spatial response fluorescence distribution. ROIs ***b–e*** were chosen within the fluorescence expression area and ROIs ***a*** and ***f*** were chosen outside the fluorescence expression area.

H): Representative ΔF/F traces from six ROIs in the field shown in (**F**).

Data are mean ± SEM. *: p< 0.05; **: p< 0.01; ***: p<0.001; ****: p<0.0001.

See also Fig. S5 for more details

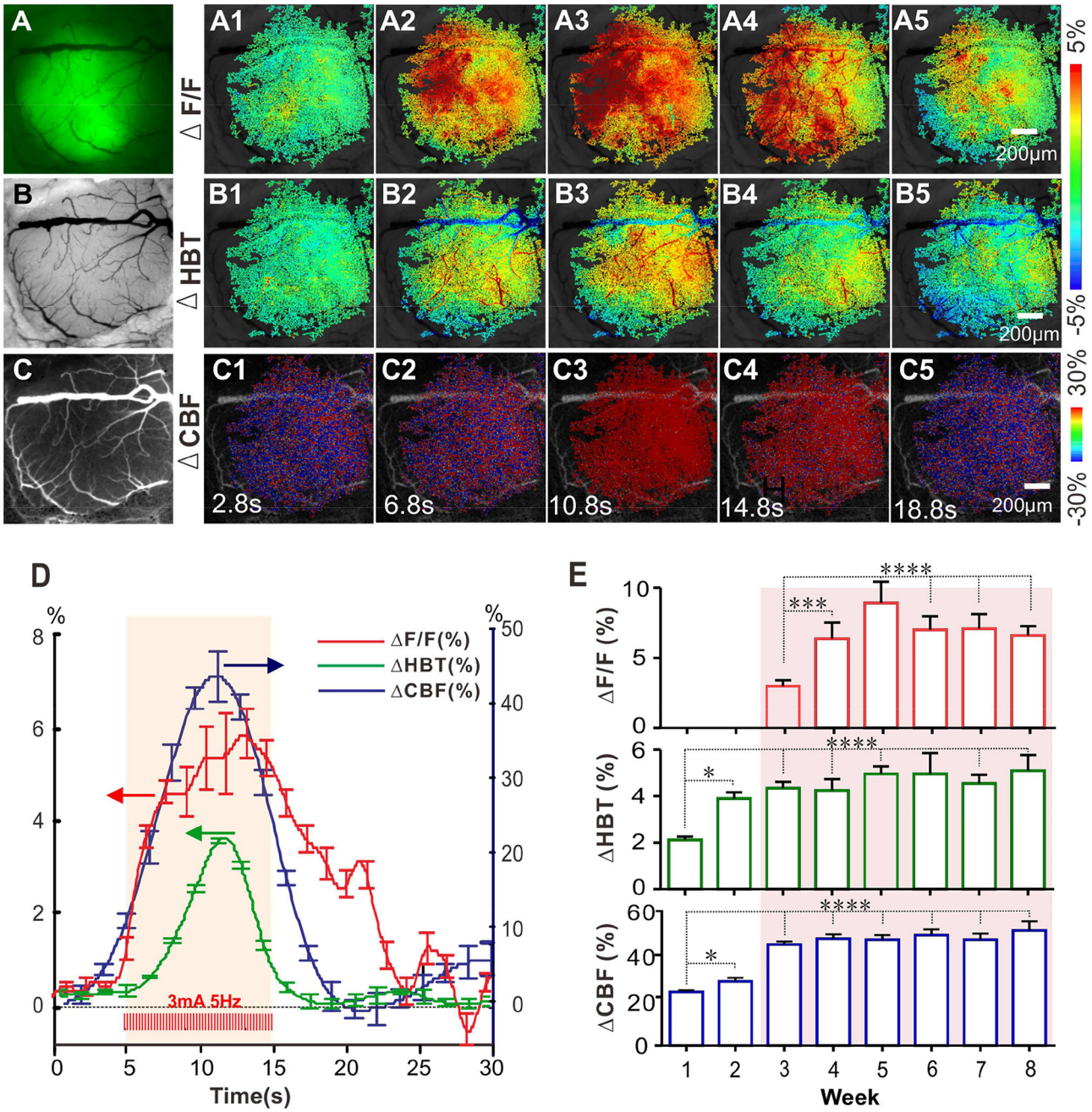

Figure 5. Multi-channel images of $[Ca^{2+}]_i$ florescence, total hemoglobin (HBT) and cerebral blood flow velocity (CBFv) changes in cortex induced by HP stimulation

A–C): The raw images obtained from a mouse cortex by using multi-channel imaging for GCaMP6f $[Ca^{2+}]_i$ fluorescence, HbT, CBFv, respectively.

A1–A5): Representative images of spatiotemporal change in G-CaMP6f fluorescence (ΔF/F) before and after HP stimulation (3mA, 5Hz, 10s).

B1–B5): Representative Images of spatiotemporal change in total hemoglobin (ΔHbT) before and after HP stimulation.

C1–C5): Representative images of spatiotemporal change in cerebral blood flow velocity (ΔCBF_V) before and after HP stimulation.

D): Mean time courses of ΔF/F, ΔHbT and ΔCBFv in response to HP stimulation (n=6), showing the temporal relationship between neuronal activity, hemodynamic response and CBF dynamics.

E): Long-term tracking of *ΔF/F, ΔHBT, ΔCBFv* peak responses from the third to the eighth week, indicating *ΔF/F, ΔHBT* and *ΔCBFv* have robust responses after the third week Data are mean ± SEM. *: $p< 0.05$; ***: $p<0.001$; ****: $p<0.0001$.

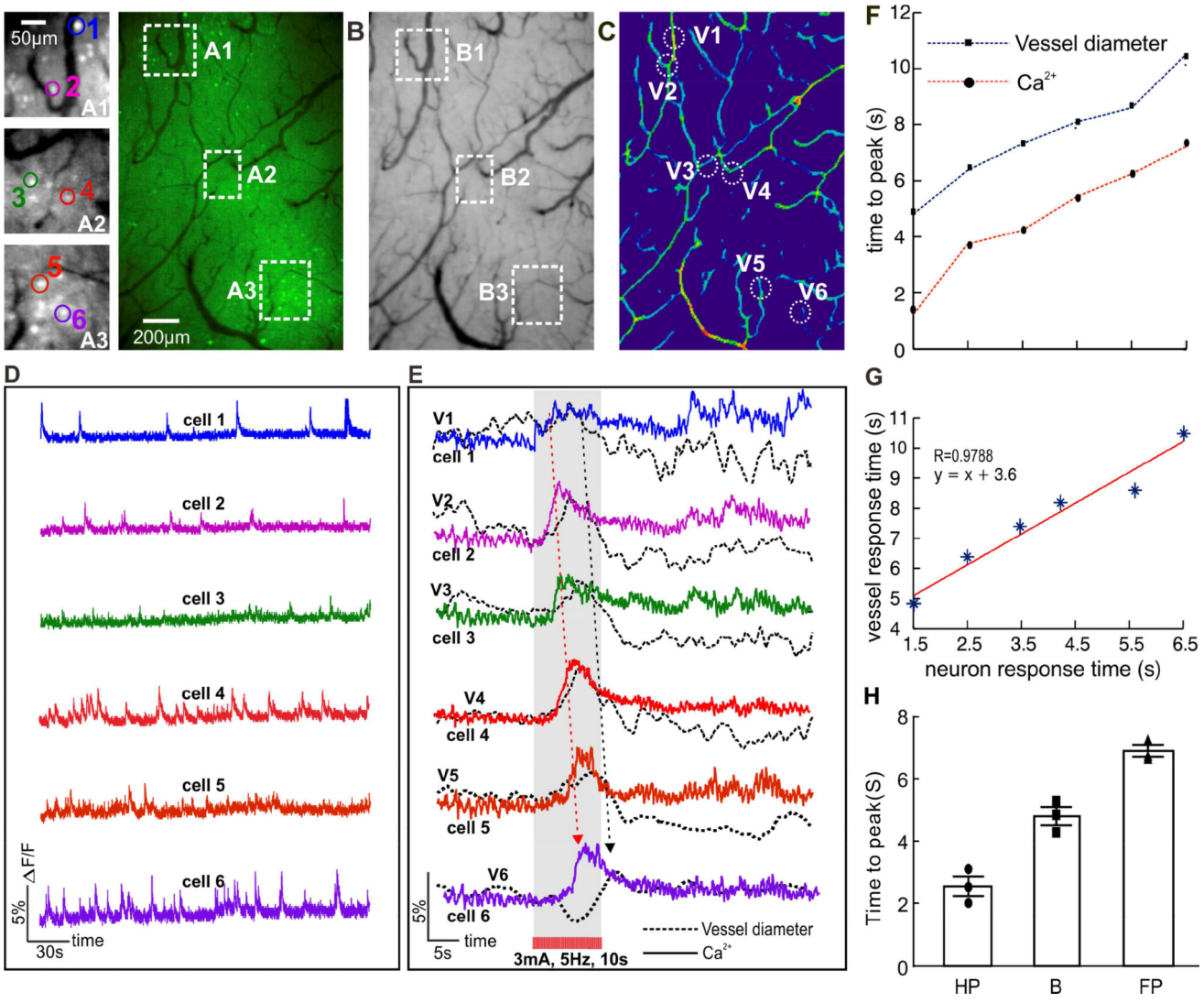

Figure 6. Simultaneous imaging of neuronal $[Ca^{2+}]_i$ activity and vascular action within cortex in response to HP stimulation. Panels

A–C): Show G-CaMP6f fluorescence and HBT images, and the vessel diameter map, respectively.

A1, A2, A3: 'Zoomed-in' images in Panel A (white box), indicating the cortical image with single neuron resolution; Number 1–6: representative Cell 1, Cell 2 till Cell 6.

B1, B2, B3: Vascular images in ROIs corresponding to A1–A3 in Panel A (white box), indicating the image with single vessel resolution.

C1, C2, C3: Calculated vessel diameter map in ROIs corresponding to B1–B3 in Panel B (white box). V1–V6: representative micro-vessels 1 to 6 near-by these neurons of A1–A6 within the ROIs.

D): Time traces of spontaneous neuronal activities for Cell 1–6, represented by the same color in Panel A.

E): Simultaneous traces of neuronal $[Ca^{2+}]_i$ changes in Cell 1–6 in response to HP stimulation (color lines) along with the diameter change of nearby micro-vessels V1–6 (black dash lines). The stars show the response peak.

F): Time to peak of the individual neurons of Cell 1–6 along with those nearby vessels (V1–6).

G): Correlation analysis of the peak time between the neurons and the micro-vessels.

H): statistical analysis of time-to-peak of [Ca^{2+}] responses in HP, B and FP to electrical-evoked HP stimulation (3mA, 5Hz, 10s). n=3.

Data are mean ± SEM. See also Fig. S5.